

PGSE NMR measurement of the non-local dispersion tensor for flow in porous media

M.W. Hunter^a, A.N. Jackson^{a,b}, P.T. Callaghan^{a,*}

^aMacDiarmid Institute for Advanced Materials and Nanotechnology, School of Chemical and Physical Sciences, Victoria University of Wellington, P.O. Box 600, Wellington 6001, New Zealand

^bThe British Library, Boston Spa, West Yorkshire, United Kingdom

ARTICLE INFO

Article history:

Received 30 November 2009

Available online 28 January 2010

Keywords:

Non-local dispersion tensor

Velocity auto correlation function

ABSTRACT

The non-local dispersion tensor provides a fundamental description of velocity correlations and displacement information in a pre-asymptotic dispersive system. Here we describe in detail how PGSE NMR may be used to measure this tensor, outlining the pulse sequences needed for signal superposition, as well as the data analysis procedures. The sequence is inherently two-dimensional, the first dimension giving the displacement resolution, the second giving correlation information. The technique is verified against simulated echo attenuation data from a lattice-Boltzmann simulation.

© 2010 Elsevier Inc. All rights reserved.

1. Introduction

The application of NMR methods to the study of fluids in porous media is now well-established. These methods include relaxation time measurement, diffusion measurement and measurement of local inhomogeneous magnetic fields. The development of new methods for understanding fluid dynamics in porous materials is important because of the wide range of applications in which such materials play a role, for example chromatography, filtration, oil recovery, catalysis, environmental waste management, groundwater flows, geothermal venting and processes relevant to animal and plant physiology. In all these applications one of the most important underlying physical phenomena is that of fluid dispersion, the process whereby molecules that start together in the same vicinity become separated as a result of translational motions. In this paper we provide details regarding a new experimental tool for the measurement of dispersion physics from a novel standpoint, that of the “non-local dispersion tensor”, whereby spatio-temporal correlations in the flow field are revealed.

Of course molecular separation, and hence dispersion, occurs in thermal equilibrium, and in the absence of fluid flow, by Brownian motion alone. In a porous medium, the presence of fluid/matrix interfaces impedes the Brownian motion so that apparent diffusion rates depend on the length and time scales used in making the measurement. But in the presence of flow, the dispersion of molecules speeds up as other mechanisms for separating initially adjacent molecules take over and the rate of dispersion rises significantly above the diffusion “baseline”. These include mechan-

ical dispersion due to stochastic variations in velocity induced by advection along tortuous paths and flow bifurcations, diffusive (Taylor) dispersion arising from molecular diffusion across streamlines and holdup dispersion which arises from the presence of dead end pores. Like diffusion, dispersion involves stochastic processes that necessitate the language of statistical physics.

A complete description of fluid behaviour is given by a knowledge of the time-dependent Eulerian flow field, in other words, the velocity $\mathbf{v}(\mathbf{r}, t)$, at all points in space and time. In principle, given infinite spatial and temporal resolution, MRI is capable of revealing this field. However, time and spatial resolution are finite and indeed traded off in MRI. By contrast, Pulsed Gradient Spin Echo (PGSE) NMR techniques which obtain an ensemble average signal from an entire sample, are ideally suited to measuring transport properties in porous media. While molecular positions are not measured in PGSE NMR, their displacements over well-defined time scales are determined. The advantage of trading away spatial localisation in such ensemble averaging is a significant gain in the available displacement length scales and time scales over which the motion may be probed.

The application of spin-echo methods to the study of flow has a long history, dating back to the original suggestion by Hahn [1], and by Carr and Purcell [2] that, in the presence of magnetic field gradients, the spin echo would be flow sensitive. In 1972, Hayward et al. [3] carried out pioneering work in the use of ensemble-averaged Pulsed Gradient Spin Echo NMR to study laminar flow in a pipe. was carried out by. In 1996 Lebon et al. [4] used PGSE NMR methods to measure the displacements of molecules in the stochastic flow as fluid was forced through a random porous medium and in 1997, Seymour and Callaghan [5] carried out an extensive PGSE NMR investigation of timescale dependence of dispersion.

* Corresponding author. Fax: +64 6 350 5164.

E-mail address: Paul.Callaghan@vuw.ac.nz (P.T. Callaghan).

Much prior PGSE NMR work has focused on attempts to measure “asymptotic dispersion”, the behaviour which applies when molecules in the flow field have moved sufficiently to sample a representative elementary volume (REV) of the locally heterogeneous porous medium, i.e., the smallest volume containing all morphological features which exist in the porous medium with their global statistical weighting [6]. Seymour and Callaghan made comparisons, with literature data from other methods, of flow-rate dependence of non-dimensionalized, asymptotic dispersion coefficients, measured transverse and longitudinal to the flow direction, while subsequent studies by other groups [7–9] extended this work.

In recent years attention has focused on flow field fluctuations that precede asymptotic dispersion. A fundamental correlation time defining the temporal structure of the velocity field is, τ_v , the duration of flow around a characteristic length scale. In general, for a medium with pore size or pore spacing given by size d , this correlation time may be written

$$\tau_v = \frac{d}{\langle v \rangle} \quad (1)$$

where, for a pore space fraction (porosity) ϕ , $\langle v \rangle = v_{tube}/\phi$, v_{tube} being the mean velocity deduced from the volume flow rate assuming that the flow area is the total cross section of the pipe. Another characteristic time, τ_D , is the time for molecules to diffuse across a pore. Using a variant of the PGSE method which allowed for independent dispersion encoding at two separated time intervals, Khrapitchev and Callaghan [10,11] made measurements of the velocity autocorrelation function, over a range of Peclet numbers, thus providing an experimental determination of τ_v . In 2007, Hunter and Callaghan [12] extended this Double PGSE method so as to measure the non-local dispersion tensor [13], thus obtaining the spatio-temporal structure of dispersive flow while at the same time preserving information regarding different directional components. The present paper presents practical details of the PGSE NMR technique used for the measurement of the non-local dispersion tensor, a quantity recognised as being of fundamental importance in the NMR characterisation of fluid dispersion [5,9,10,14–21].

In what follows we describe the non-local dispersion tensor and provide a detailed description the NMR method used for its measurement including the signal superposition method, as well as the data analysis procedures. We demonstrate the method experimentally for dispersive, low Reynolds number (Re), flow in a random bead pack of mono-sized spheres. In order to test our NMR method independently, we have carried out a lattice-Boltzmann simulation of the flow field through an independently generated beadpack. This flow field is used to simulate dispersion by allowing virtual tracer particles to flow and diffuse through the pore space. These tracers can then be used to estimate the non-local dispersion tensor in the simulated flow. The same code can also be used to simulate the NMR experiment, thus providing a means of comparing the tensor that results from the NMR data analysis protocol with that obtained from the tracer particle analysis.

2. The non-local dispersion tensor

To explain the non-local dispersion tensor, it is helpful to begin by defining a steady state Eulerian flow field $\mathbf{v}_E(\mathbf{r}, t) = \mathbf{v}_E(\mathbf{r})$ and a stationary Lagrangian flow ensemble $\mathbf{v}_L(t)$ with mean flow $\langle \mathbf{v} \rangle$. The fluctuating (zero mean) parts of the velocities, $\mathbf{u}_E(\mathbf{r})$ and $\mathbf{u}_L(t)$ are thus defined by

$$\mathbf{v}_E(\mathbf{r}) = \mathbf{u}_E(\mathbf{r}) + \langle \mathbf{v} \rangle \quad (2)$$

and

$$\mathbf{v}_L(t) = \mathbf{u}_L(t) + \langle \mathbf{v} \rangle \quad (3)$$

The asymptotic dispersion tensor, \mathbf{D}^* , is described in terms of the velocity autocorrelation function (VACF) of the Lagrangian velocities by [13,22]

$$\mathbf{D}^* = \lim_{t \rightarrow \infty} \text{sym} \int_0^t d\tau \langle \mathbf{u}_L(0) \mathbf{u}_L(\tau) \rangle \quad (4)$$

where $\langle \dots \rangle$ represents the Lagrangian ensemble average. Note that \mathbf{D}^* may also be defined in Einsteinian terms involving the dyadic of mean square displacements, $\sigma^2(t)$ by [22]

$$\mathbf{D}^* = \lim_{t \rightarrow \infty} \frac{1}{2} \frac{d\sigma^2}{dt} \quad (5)$$

While the VACF is naturally describes in terms of the Lagrangian ensemble of velocities, it can be easily linked with the Eulerian field via a propagator $P(\mathbf{r}|\mathbf{r}', \tau)$ which describes the conditional probability that a fluid element initially at \mathbf{r} will migrate to \mathbf{r}' at a later time τ . $P(\mathbf{r}|\mathbf{r}', \tau)$ is governed by the microscale advection–diffusion equation for the system. For any given starting probability $P(\mathbf{r}, 0)$, the velocity autocorrelation function can then be written

$$\langle \mathbf{u}_L(0) \mathbf{u}_L(\tau) \rangle = \int d\mathbf{r}' \int d\mathbf{r}_E(\mathbf{r}, 0) P(\mathbf{r}, 0) P(\mathbf{r}|\mathbf{r}', \tau) \mathbf{u}_E(\mathbf{r}', \tau) \quad (6)$$

The integral over time in Eq. (4) means that details of the VACF temporal correlations are buried in the asymptotic dispersion tensor. Similarly, the integral $\int d\mathbf{r}_E(\mathbf{r}, 0) P(\mathbf{r}, 0) P(\mathbf{r}|\mathbf{r}', \tau) \mathbf{u}_E(\mathbf{r}', \tau)$ contains spatial correlation information buried in the VACF. This is known as the non-local dispersion tensor [13] and is a primary quantity of interest in any detailed description of dispersive flow. We may conveniently rewrite this quantity in terms of relative displacements in time and space we may define the non-local dispersion tensor, the VACF, and the asymptotic dispersion by

$$\mathbf{D}^{NL}(\mathbf{R}, \tau) = \int d\mathbf{r}_E(\mathbf{r}, 0) P(\mathbf{r}) P(\mathbf{r}|\mathbf{r} + \mathbf{R}, \tau) \mathbf{u}_E(\mathbf{r} + \mathbf{R}, \tau) \quad (7)$$

and

$$\langle \mathbf{u}_L(0) \mathbf{u}_L(\tau) \rangle = \int d\mathbf{R} \mathbf{D}^{NL}(\mathbf{R}, \tau) \quad (8)$$

and

$$\mathbf{D}^* = \lim_{t \rightarrow \infty} \text{sym} \int_0^t d\tau \int d\mathbf{R} \mathbf{D}^{NL}(\mathbf{R}, \tau) \quad (9)$$

We have shown [12] that the tensor $\mathbf{D}^{NL}(\mathbf{R}, \tau)$ can be directly measured using PGSE NMR. The key to this measurement is to not only encode the NMR signal with information concerning the displacement propagator, but to ensure that the experiment is also sensitive to velocities separated in space and time. The details of our approach are as follows.

3. NMR implementation

3.1. The pulse sequence

We begin with the pulse sequences shown in Fig. 1. Each is two-dimensional in encoding gradient, and the signal superposition resulting from this pair enable extraction of the components of the non-local dispersion tensor. The first sequence shown in Fig. 1(a) is termed “compensated” since mean flow effects are nulled in the double-PGSE dimension, while that shown in 1(b) is uncompensated resulting in a net phase shift due to mean flow. Note that as shown, with unique phases for the RF pulses, each of these sequences contain a superposition of compensated and uncompensated phase terms arising from the flow. In order to ensure that pure compensated and uncompensated phase shifts result, an appropriate RF phase cycle is required.

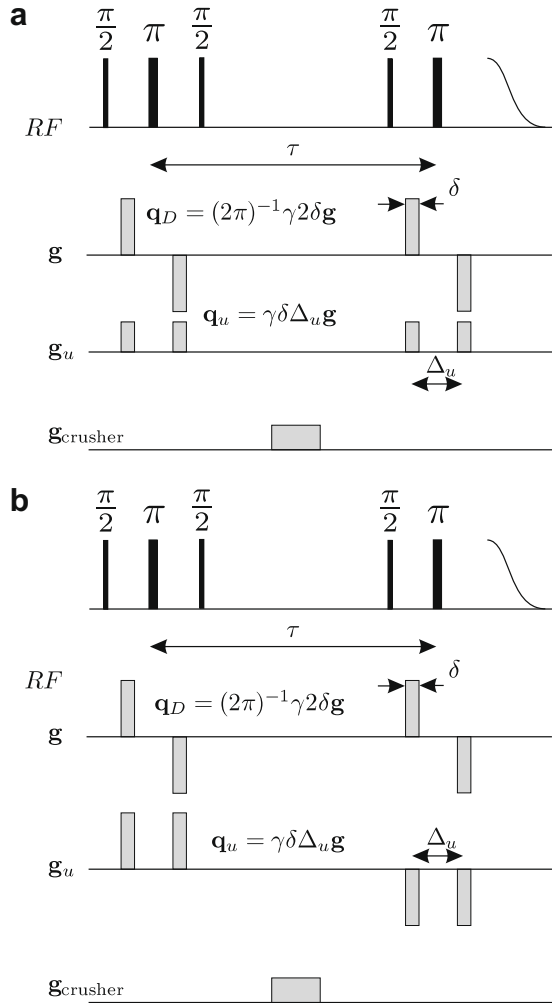


Fig. 1. The ‘compensated’ (a) and ‘uncompensated’ (b) versions of the pulse sequence. A superposition is required when post-processing the signal.

Note that the encoding dimensions, \mathbf{q}_D and \mathbf{q}_u relate, respectively, to the dynamic displacement \mathbf{R} and the local velocity \mathbf{v} . The data analysis and pulse implementation for each dimension is different. Analysis in the displacement dimension requires the displacement encoding to be in the propagator sense, so that full attenuation is achieved and the propagator information can be recovered via a Fourier transform. This encoding is implemented using a Bi-Polar PGSE [23] with each pulse having a strength \mathbf{g} and a duration of δ . By contrast, in order to get the necessary velocity encoding in the second dimension, the experiments must be performed and analysed in the low- q limit, as previously used in measurements of the VACF using double-PGSE experiments [10]. Each pair of gradients, with a strength of \mathbf{g}_u and duration of δ are separated by a time Δ_u . Note that our definition of q will be different for the two dimensions: in the displacement dimension $\mathbf{q}_D = (2\pi)^{-1}\gamma 2\delta\mathbf{g}$ such that q is the Fourier conjugate of displacement, and in the velocity encoding dimension \mathbf{q}_u is the phase conjugate of velocity such that $\mathbf{q}_u = \gamma\delta\Delta_u\mathbf{g}_u$ where γ is the magnetogyric ratio. The two dimensions of gradient pulses are generally implemented concurrently with the same pulse duration, δ , such that when the displacement and velocity encoding directions are the same, the gradient pulses superpose.

The time τ which denotes the separation of the double PGSE pulses represents a ‘mixing-time’ in the NMR sense. This time provides the temporal dimension for fluctuations in the velocities,

essentially the timescale for velocity correlation. Of course, while our pulse sequence is a double PGSE with regards to velocity encoding, in a displacement sense, it is set up as a single PGSE encoding, and we will refer to τ as an ‘encoding-time’ in that context.

3.2. The NMR signal

The normalised signal acquired at the final spin echo from the sequence shown in Fig. 1a may be written

$$E(\mathbf{q}_D, \mathbf{q}_u) = \int \int \exp(i2\pi\mathbf{q}_D \cdot \mathbf{R}) \exp(-i\mathbf{q}_u \cdot (\mathbf{u}_E(\mathbf{r}, 0) + \langle \mathbf{v} \rangle)) \times P(\mathbf{r})P(\mathbf{r}|\mathbf{r} + \mathbf{R}, \tau) \exp(i\mathbf{q}_u \cdot (\mathbf{u}_E(\mathbf{r} + \mathbf{R}, \tau) + \langle \mathbf{v} \rangle)) d\mathbf{R}d\mathbf{r} \quad (10)$$

taking the inverse Fourier transform in the \mathbf{q}_D dimension, $\mathcal{F}_{\mathbf{q}_D}^{-1}\{\dots\}$, gives us an expression we call S , a function of \mathbf{R} and \mathbf{q}_u ,

$$S(\mathbf{R}, \mathbf{q}_u) = \mathcal{F}_{\mathbf{q}_D}^{-1}\{E(\mathbf{q}_D, \mathbf{q}_u)\} = \int \exp(-i\mathbf{q}_u \cdot \mathbf{u}_E(\mathbf{r}, 0))P(\mathbf{r})P(\mathbf{r}|\mathbf{r} + \mathbf{R}, \tau) \times \exp(i\mathbf{q}_u \cdot \mathbf{u}_E(\mathbf{r} + \mathbf{R}, \tau))d\mathbf{r} \quad (11)$$

Note that the integral over starting position $\int \dots d\mathbf{r}$ can be also be represented by an ensemble average notation $\langle \dots \rangle$. The displacement information is implied through the average propagator $\bar{P}(\mathbf{R}, \tau)$ so that S becomes

$$S(\mathbf{R}, \mathbf{q}_u) = \langle \exp(-i\mathbf{q}_u \cdot \mathbf{u}_E(0))\bar{P}(\mathbf{R}, \tau) \exp(i\mathbf{q}_u \cdot \mathbf{u}_E(\tau)) \rangle \quad (12)$$

Using this ensemble average notation we can write the non-local dispersion tensor compactly as

$$\mathbf{D}^{NL}(\mathbf{R}, \tau) = \langle \mathbf{u}_E(0)\bar{P}(\mathbf{R}, \tau)\mathbf{u}_E(\tau) \rangle \quad (13)$$

Henceforth the subscripts denoting Eulerian velocities will be omitted and compact notation of equation in Eq. (13) employed. However the strict definitions are as given in Eqs. (7) and (11).

3.3. The low- q limit

In the analysis of our echo attenuation data, the Fourier transformation with respect to \mathbf{q}_D represents the first step, so that subsequent analysis is performed on $S(\mathbf{R}, \mathbf{q}_u)$. To obtain the desired expression for \mathbf{D}^{NL} we need to expand the echo attenuation, in the q_u dimension, in the low- q limit. Taking, for example, the direction of displacement encoding and velocity encoding to be both in the Z direction (also chosen as the direction of the tube velocity), we get for the first version of the pulse sequence in which the phase shift due to the bulk flow is compensated,

$$S_{comp}(Z, q_u) = \left\langle \left(1 - iq_u u_z(0) - q_u^2 \frac{u_z(0)^2}{2} + iO(q_u^3) + O(q_u^4) \right) \bar{P}(Z, \tau) \times \left(1 + iq_u u_z(\tau) - q_u^2 \frac{u_z(\tau)^2}{2} - iO(q_u^3) + O(q_u^4) \right) \right\rangle$$

where q_u represents the magnitude of a \mathbf{q}_u vector applied along the z -axis.

Expanding in q_u we have

$$S_{comp}(Z, q_u) = \bar{P}(Z, \tau) + iq_u \langle u_z(0)\bar{P}(Z, \tau) \rangle - \frac{q_u^2}{2} \langle u_z(0)^2\bar{P}(Z, \tau) \rangle - iq_u \langle \bar{P}(Z, \tau)u_z(\tau) \rangle - q_u^2 \langle u_z(0)\bar{P}(Z, \tau)u(\tau) \rangle - \frac{q_u^2}{2} \langle \bar{P}(Z, \tau)u_z(\tau)^2 \rangle + iO(q_u^3) + O(q_u^4) \quad (14)$$

Because the real and imaginary parts of the data are independently handled, it is necessary to account separately for the truncation

errors in q_u^3 and q_u^4 . The tensor elements which we seek are present as partial coefficients of q_u^2 . Note that the velocities in the correlation term in Eq. (12) are denoted as being separated in time by τ because of the experimental encoding for the propagator. For terms involving velocity, but without correlation at separated times, the apparent time dependence of u_z may be dropped.

The second version of the pulse sequence is termed uncompensated. It is performed with the sign of the second velocity encoding pulse reversed as shown in Fig. 1b, and yields

$$\begin{aligned} S_{uncomp}(Z, q_u) = \exp(i2q_u\langle v_z \rangle) & \left(\bar{P}(Z, \tau) + iq_u\langle u_z \bar{P}(Z, \tau) \rangle \right. \\ & - \frac{q_u^2}{2} \langle u_z^2 \bar{P}(Z, \tau) \rangle + iq_u \langle \bar{P}(Z, \tau) u_z \rangle \\ & + q_u^2 \langle u_z(0) \bar{P}(Z, \tau) u_z(\tau) \rangle \\ & \left. - \frac{q_u^2}{2} \langle \bar{P}(Z, \tau) u_z^2 \rangle + iO(q_u^3) + O(q_u^4) \right) \end{aligned} \quad (15)$$

Because of the lack of compensation for mean flow, an extra phase factor, $\exp(i2q_u\langle v_z \rangle)$ is present at the beginning of the expression. This factor is easily determined by examining the data $E(0, q_u)$ and can be retrospectively corrected. With this correction and with a difference superposition we have

$$\begin{aligned} S_{comp}(Z, q_u) - \exp(-i2q_u\langle v_z \rangle) S_{uncomp}(Z, q_{uz}) \\ = i2q_u \langle \bar{P}(Z, \tau) u_z \rangle + 2q_u^2 \langle u_z(0) \bar{P}(Z, \tau) u_z(\tau) \rangle + iO(q_u^3) + O(q_u^4) \end{aligned} \quad (16)$$

Thus the elements of the non-local dispersion tensor may be obtained from this superposition by fitting the real part to the q_u^2 dependence in the low- q limit.

3.4. Extracting D^{NL}

Other elements of the non-local tensor may be obtained by different choices for the directions of \mathbf{q}_D and \mathbf{q}_u . Note that the choices of directions for the initial and final velocity encoding need not be coincident. Eq. (16) can be generalised using the dimension subscripts α and β for the initial and final velocity, and γ , for the direction of the displacement, denoted X with the appropriate subscript. The non-local dispersion tensor, written in this subscript form is

$$D_{\alpha\beta}^{NL}(X_\gamma, \tau) = \langle u_\alpha(0) \bar{P}(X_\gamma, \tau) u_\beta(\tau) \rangle \quad (17)$$

Omitting the truncation errors, a general form for the superposition is

$$\begin{aligned} \exp(iq_{u\alpha}\langle v_\alpha \rangle - iq_{u\beta}\langle v_\beta \rangle) S_{comp}(X_\gamma, q_{u\alpha,\beta}) - \exp(iq_{u\alpha}\langle v_\alpha \rangle \\ + iq_{u\beta}\langle v_\beta \rangle) S_{uncomp}(X_\gamma, q_{u\alpha,\beta}) \\ = iq_{u\alpha}\langle u_\alpha \bar{P}(X_\gamma, \tau) \rangle + iq_{u\beta}\langle \bar{P}(X_\gamma, \tau) u_\beta \rangle \\ + 2q_{u\alpha}q_{u\beta}\langle u_\alpha(0) \bar{P}(X_\gamma, \tau) u_\beta(\tau) \rangle \end{aligned} \quad (18)$$

where $q_{u\alpha,\beta}$ means the first pair of velocity encoding gradients are along α and the second along β .

In cases where the velocity encoding is in a direction that has no bulk flow, no phase correction is necessary whereas, if the initial and final motion encodings are orthogonal and only one is component is parallel to the direction of the main flow, z , the phase correction factor is $\exp(-iq_u\langle v \rangle)$ and appears in both $S_{comp}(X_\gamma, q_{u\alpha,z})$ and $S_{uncomp}(X_\gamma, q_{u\alpha,z})$. Despite the fact the neither pulse sequence is uncompensated or compensated, the oppositely signed \mathbf{q}_u encodings still provide the appropriate superposition. If the phase correction is omitted, the resulting superposition will give tensors not in u , but in v .

Eq. (18) contains terms linear in \mathbf{q}_u . In handling these, two experimental strategies are possible. In the first a further superpo-

sition using $S_{comp}(X_\gamma, -q_{u\alpha,\beta})$ and $S_{uncomp}(X_\gamma, -q_{u\alpha,\beta})$ is performed to eliminate the q term. In the second the real and the imaginary parts of the data can be treated separately thus allowing the additional extraction of the two ensemble averages $\langle u_\alpha P(X_\gamma) \rangle$ and $\langle u_\beta P(X_\gamma) \rangle$.

The three choices of directions available for the three different encodings give a total of 27 terms. There are six, non-zero, independent terms for flow in a porous medium.

4. Experimental method

PGSE NMR experiments were performed using a Bruker AVANCE 400 MHz spectrometer equipped with a microimaging gradient set capable of providing 1.45 T m^{-1} . A bead pack column consisting of randomly packed $500 \mu\text{m}$ latex monodisperse spheres was contained in a poly(ether ether ketone) (PEEK) cylinder of inner diameter 10 mm and distilled, degassed water was pumped (BVP-Z Ismatec) through. The beadpack was contained by plugs of porous plastic, outside the sensitive region of the rf coil (a 'birdcage' resonator with a diameter of 15 mm), to a length of 50 mm. The porosity of the beadpack was measured from a T_2 compensated one-dimensional image of a partially filled beadpack. The porosity was found to be $(37.5 \pm 0.5)\%$.

In order to dampen out high-frequency pulsations from the pump, a length of rubber tubing was used in series with the otherwise teflon tubing. This is an essential part of the experiment since the sensitive velocity encoding that make up the double PGSE component are performed over 2–3 ms, and separated by 10 s of ms. The total experiment time take several hours, hence the need to a stable flow over a wide range of time scales. Any remaining variation in the flow was not detrimental to the signal quality. The liquid was pumped at a tube velocity of around 10.2 mm s^{-1} , giving a τ_v of 49.0 ms, a Peclet number of approximately 1500 and a Reynolds number of approximately 3.3. Experiments reported here are performed at displacement encoding times of 10 ms, 21.5 ms and 46.3 ms. The spacing, Δ_u , between each double-PGSE pair was 2 ms, ensuring $\Delta_u \ll \tau_v$. To reduce the delay between scans, caused by the need to allow for near-complete T_1 relaxation, the water was doped by 0.025 wt% with GdCl_3 to give a T_1 of approximately 110 ms.

4.1. Pulse sequence

The use of a BP-PGSE encoding for the displacement is not strictly necessary since the expected internal gradients for our bead pack are small. However, the low attenuation due the motion encoding pulses was more reliable when the pulses were separated by at π pulse and so the displacement encoding pulses were similarly implemented.

Typically in a BP-PGSE experiment, unwanted phase coherences due to the π pulses can be minimised by using small crusher gradients either side of the rf pulse. These crusher gradients would normally be in a direction orthogonal to the main encoding. It is usually assumed that any attenuation caused by these gradients are small compared to the effects being measured. However in this case we do not have this freedom as it is precisely the small effects we are expecting to measure with the low- q motion encoding pulse. To this end we need a comprehensive 32-step phase cycle to minimise the unwanted coherence. The complete phase cycle is given in Table 1.

Note that the phase cycle performs two separate tasks. First, it removes baseline artifacts and the unwanted FIDs generate by all RF pulses other than the first $\frac{\pi}{2}$ excitation pulse. Second, it ensures that the appropriate superposition of orthogonal transverse plane magnetisation components are stored, so as to produce the desired pure phase shift term after recall following the storage period.

The signal averaging that accompanies the 32 steps in the phase cycle is advantageous when fitting in the low- q dimension, and

Table 1

The 32-step phase cycle for the pulse sequence depicted in Fig. 1. This phase cycle minimises unwanted coherences without the need for crusher gradients around the π pulses and also ensures pure phase-encoded terms after recall following the storage period.

| | | | | | | | | |
|------------|--------|----------|--------|----------|----------|----------|----------|----------|
| Excitation | xxxx | xxxx | xxxx | xxxx | -x-x-x-x | -x-x-x-x | -x-x-x-x | -x-x-x-x |
| π | yyyy | -y-y-y-y | yyyy | -y-y-y-y | yyyy | -y-y-y-y | yyyy | -y-y-y-y |
| Storage | x-xy-y | x-xy-y | x-xy-y | x-xy-y | -xx-yy | -xx-yy | -xx-yy | -xx-yy |
| Recall | x-xy-y | x-xy-y | -xx-yy | -xx-yy | x-xy-y | x-xy-y | -xx-yy | -xx-yy |
| π | y-y-xx | y-y-xx | y-y-xx | y-y-xx | y-y-xx | y-y-xx | y-y-xx | y-y-xx |
| Receiver | xx-x-x | xx-x-x | -x-xxx | -x-xxx | -x-xxx | -x-xxx | xx-x-x | xx-x-x |

gives the opportunity for improved displacement resolution in the propagator. For some encoding times there is still a small amount of unwanted signal when $q_u = q_D = 0$. This results in an offset at $q_u = 0$ in $S(X_\gamma, q_u)$. The low- q fit algorithm can easily ignore this point.

4.1.1. Displacement encoding

The acquisition in the displacement dimension is performed using a grained approach [24], typically in three stages. This enabled sharp resolution of any stagnant or slow moving peak while still capturing the faster moving particles. If the encoding was in the longitudinal direction the displacement encoding was performed using 22 fine, 14 medium and 26 course increments between equal positive and negative gradients giving a total of 63 gradient values. The step ratios were 1:2:8 giving an interpolated data set with 259 values, the first 258 were used for the discrete Fourier transform. Fig. 2 shows the measured and interpolated q_D data for an experiment with displacement encoding direction, Z, parallel to the main flow. With the exception of Figs. 8 and 10 all the examples shown here will be from the same pair of experiments, that which is needed for extracting $D_{zz}^{NL}(Z, \tau)$ for $\tau = 46.3$ ms. For transverse encoding only a two stage graining was required 14 medium and 26 course increments giving a total of 41 steps. The step ratios were 1:4 giving an interpolated data set with 119 values. Fig. 3(a) and (b) show that all the fine structure of the echo attenuation is resolved, this is also true when the echo attenuation is expanded into the q_u dimension.

The interpolation was performed using in logarithmic space for the magnitude of the echo attenuation and a linear interpolation for the phase of the echo attenuation, these were then combined to give the conventional real and imaginary parts of the echo attenuation. No zero-filling, symmetrising or filtering was required in this dimension.

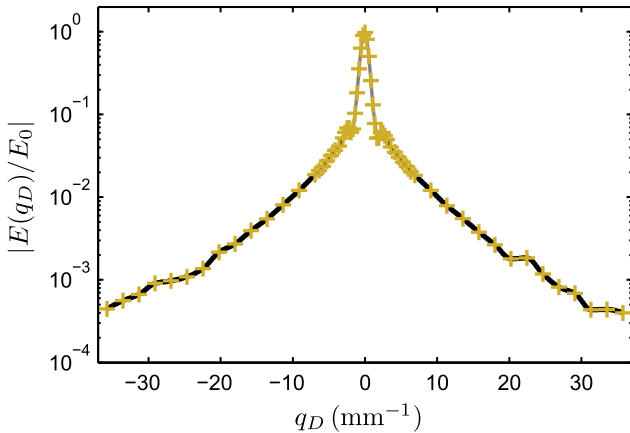


Fig. 2. The magnitude of the echo attenuation for a longitudinal displacement encoding when $q_u = 0$. In this case $\tau = 46.3$ ms. The yellow crosses show measured data and the black dots show the interpolated data. The signal is fully attenuated at maximum q giving a signal to noise of around 1000. (For interpretation of color mentioned in this figure the reader is referred to the web version of the article.)

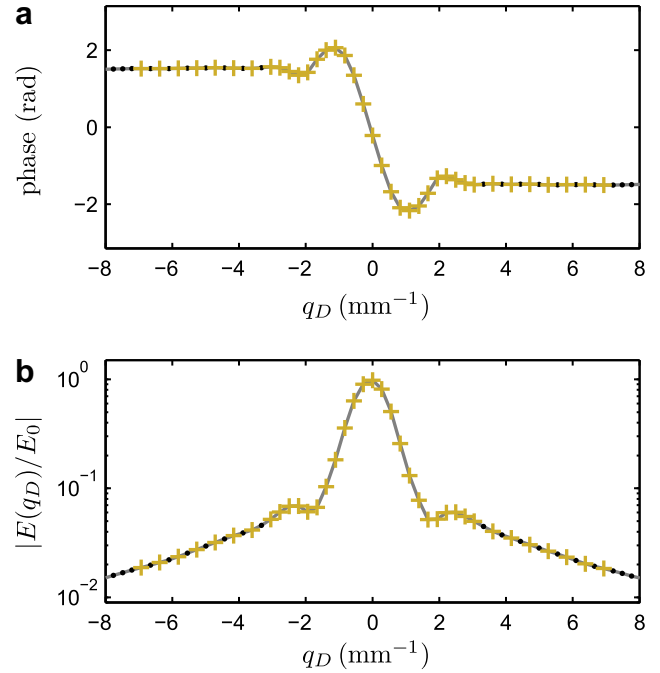


Fig. 3. The measured and interpolated data around $q_D = 0$ for the encoding described in Fig. 2. The yellow crosses show measured data and the black dots show the interpolated data. The gray line acts as a guide for the eye. The fine structure is resolved both in the phase and the magnitude. (For interpretation of color mentioned in this figure the reader is referred to the web version of the article.)

4.1.2. Motion encoding

The motion encoding is performed using a pair of gradients around a π pulse separated by Δ_u . To increase the reliability of the gradient pairs, 1–3 ‘warm-up’ pulse-pairs were used, both before the main excitation pulse and during the storage period. For short mixing times this was not practical. For measurement of components where motion and displacement were in the same direction, the superposition of the gradient pulses were used in the ‘warm-up’ train.

Omitting the ‘warm-up’ pulses has little effect on the magnitude of the echo attenuation but it does introduce an artifact of a q_u dependent phase shift. At first this is not seen as a problem since the q_u dependent phase shift is compensated as is the ‘real’ q_u dependent phase shift due to the bulk velocity. However when tensors in v are to be examined this artifact needs to be minimised, either by using the ‘warm-up’ pulses or by comparing the phase shift to that measured with no flow.

Eq. (16) suggests the q^2 fit should be performed after the superposition, however in practice the fitting is done beforehand. Treating the compensated and uncompensated experiments separately in this way enables independent choice of maximum motion encoding gradients. Typically 21–33 q_u steps are used to give reliable low- q fits. The total time for the pair of experiments necessary for one measurement is around 8 h for transverse encodings and 12 h for longitudinal.

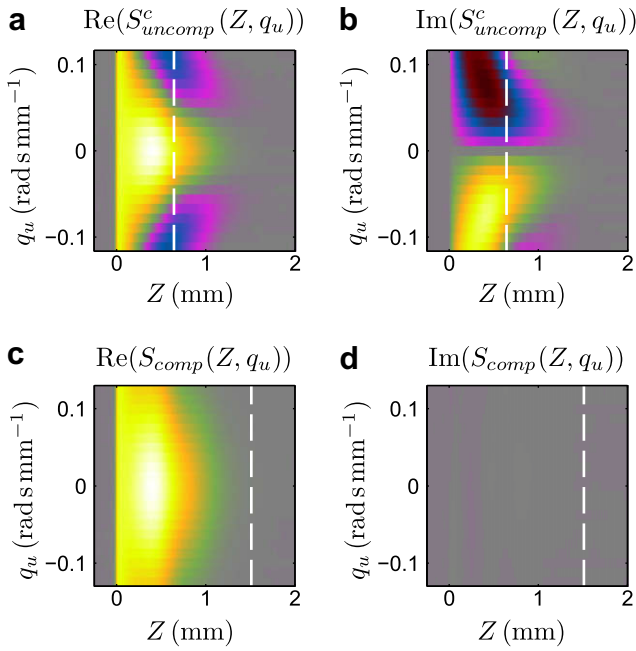


Fig. 4. The real (a) and imaginary (b) parts of S_{uncomp}^c and the real (c) and imaginary (d) parts of S_{comp} . These are the two data sets necessary to give $D_{zz}^{NL}(Z, \tau)$. In this case $\tau = 46.3$ ms. The dotted white lines in panels (a) and (b) show the displacement pixels chosen to as an example of the q^2 fitting in Fig. 5 and the line in panels (c) and (d) show the displacement pixel used in Fig. 6. The amplitude of S_{comp} at the chosen displacement pixel is not resolved in the color map above. (For interpretation of color mentioned in this figure the reader is referred to the web version of the article.)

4.2. Post processing

The phase correction factor in Eq. (15), is found from examining phase shift of the echo attenuation $E(q_D, q_u)$ at $q_D = 0$. The linear term from a cubic fit is used for evaluation. The phase corrected $S(X_\gamma, q_u)$ from the uncompensated experiment will be denoted by $S_{uncomp}^c(X_\gamma, q_u)$.

The superposition to find D^{NL} relies on the validity of the low- q approximation. Previous use of this technique has been used to investigate the VACF [10] and typically this approximation has been held to be true if the attenuation is $0.7E_0$, points outside of this range were ignored and a linear fit in q^2 was made to the remainder of the data. Tests using a fit to more attenuation showed similar characteristics [10].

In non-local dispersion experiments, however, once each data set is Fourier transformed giving S , the variations in $S(X_\gamma, q_u)$ for

each displacement pixel can be quite extreme. Fig. 4 shows examples of $S_{comp}(Z, q_u)$ and $S_{uncomp}^c(Z, q_u)$. To provide a reliable estimate for the q_u^2 coefficient we need an algorithm that is relatively independent of the resulting attenuation.

For each displacement pixel of $S(Z, q_u)$ the low- q fit was performed by first fitting an even polynomial to the magnitude and then an odd polynomial to the phase, from these the coefficients of q^0 , q^1 and q^2 from expressions (14) and (15) can reliably be estimated.

To enable the algorithm to be relatively insensitive to attenuation but also stable, a multi-stage process was used. Beginning with $N = 8$, a N th order even polynomial was fitted to the magnitude. The fit was rejected if the standard error in the N th order term was greater than the magnitude of the N th order term. A $(N - 2)$ th order fit was then tested under the same criteria until a fit to the magnitude is found. This algorithm will typically use a 6th order fit for the q_u data with large attenuations ($\sim 0.2S(X_\gamma, q_u = 0)$), and usually will not false fit a higher order polynomial to noise. Once the magnitude fit has been found, this is used to estimate the q value, q_a that gives an attenuation of $0.7E_0$, allowing the definition of a weight function

$$wt = \frac{1}{\left(1 + \exp\left(-\frac{A}{q_a}(q + q_a)\right)\right)\left(1 + \exp\left(\frac{A}{q_a}(q - q_a)\right)\right)} \quad (19)$$

which is essentially a broadened hat function where the factor A , typically 10, determines the width of the broadening. The same polynomial fit is then performed with the weight function, thus reducing the truncation error of the fit and determining the points that we consider to fulfill the low- q approximation. If the point q_a can not be estimated, no weight function is used. This is typically the case for low attenuation in the q_u direction of $S(X, q_u)$ and would usually result in a low order polynomial fit.

The q_u dependent phase is fitted in a similar a fashion. Using the weight function determined above, beginning with a fifth order odd polynomial until an acceptable fit is found. This phase shift is significant in the uncompensated experiment and is zero within experimental artifacts for the compensated experiment, nevertheless the same algorithm is used to perform a fit, usually resulting in a linear fit with a small q_u dependent term. With the two polynomial fits, the curvature of the real data around $q_u = 0$ can be determined, with an estimate of the error.

Figs. 5 and 6 show examples of the fitting algorithm for the uncompensated and compensated experiments respectively. The uncompensated example is for a displacement near the average where signal to noise is excellent. The q_u dependent phase shift can clearly be seen in panels (c) and (d). The complex polynomial

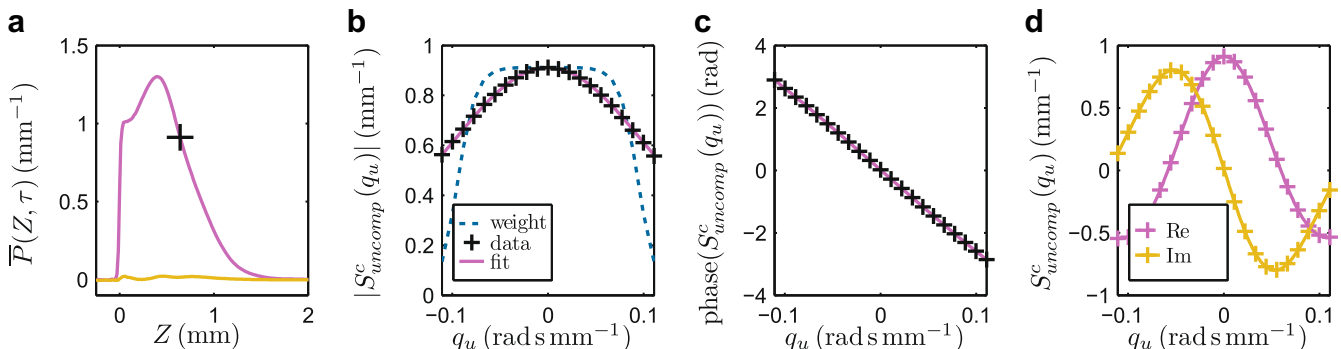


Fig. 5. The low- q fitting to the phase corrected uncompensated encoding for $D_{zz}^{NL}(Z, \tau)$, $\tau = 46.3$ ms. The full data set is shown in Fig. 4(a) and (b). The magnitude of the q_u attenuation showing the data shown in panel (b), at the displacement pixel marked by a black cross on the propagator in panel (a). Panel (b) also shows the weight function (dotted blue line) used to perform the fit, shown in purple, of the magnitude and phase, panels (b) and (c) respectively. Panel (d) shows the complete fit to the q_u data from which the q_u^2 coefficient can be estimated. (For interpretation of color mentioned in this figure the reader is referred to the web version of the article.)

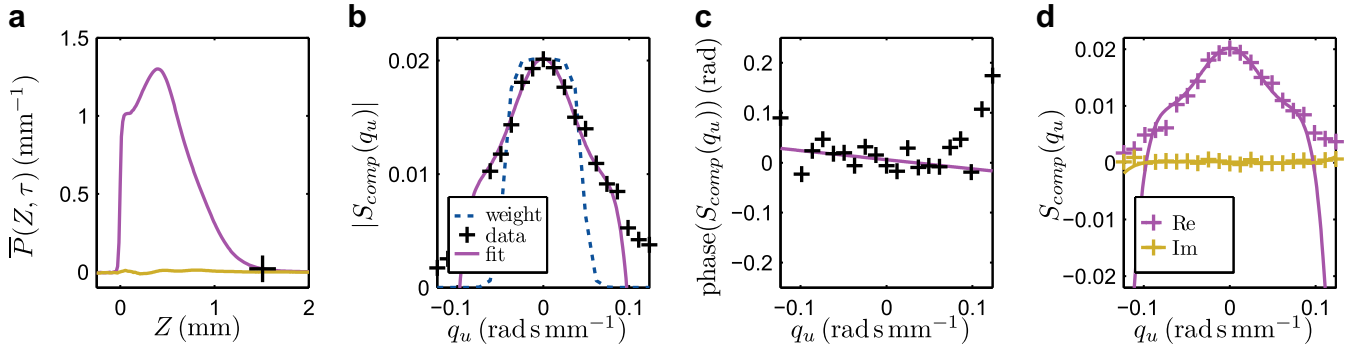


Fig. 6. The low- q fitting to the compensated encoding for $D_{zz}^{NL}(Z, \tau)$, $\tau = 46.3$ ms. The full data set is shown in Fig. 4(c) and (d). The magnitude of the q_u attenuation showing the data shown in panel (b), at the displacement pixel marked by a black cross on the propagator in panel (a). In this example the displacement is large giving poor signal to noise. Panel (b) also shows the weight function (dotted blue line) used to perform the fit, shown in purple, of the magnitude and phase, panels (b) and (c) respectively. Panel (d) shows the complete fit to the q_u data from which the q_u^2 coefficient can be estimated. Clearly the weight function prevents an accurate fit to the complete data but still provides a reliable fit to the data around $q_u = 0$. (For interpretation of color mentioned in this figure the reader is referred to the web version of the article.)

fit to the data in panel (d) allows the coefficients of q and q^2 to be determined. In this case the fit to the phase was a 5th order odd polynomial and to the magnitude was a fourth order even polynomial. The compensated example in Fig. 6 is for a large displacement, such that the signal to noise is poor. In this example the proportion of particles moving this distance is 0.02%. The weight function largely ignores the points at large q_u but the fit in panel (d) still shows good agreement around $q_u = 0$. The magnitude was fitted with a 6th order polynomial and the phase was fitted with a linear polynomial.

Once the fitting has been performed for each displacement pixel the superposition can be performed. Fig. 7 continues with our example of $D_{zz}^{NL}(Z, \tau)$. In this case the differences between the two

encoding is relatively large, thus giving small error bars. The need for noise insensitive, robust algorithm is highlighted in other cases, such as in the superposition required for the encoding describing transverse displacement and velocity correlations, $D_{xx}^{NL}(X, \tau)$ for $\tau = \tau_p$. Fig. 8 shows a very small difference between the fitted data sets.

A superposition can also be made to extract various other tensors. These terms do not contain any information correlating velocities in space and time, but do give structure and temporal information to the first and second moments $\langle u_z \rangle$ and $\langle u_z^2 \rangle$. The phase correction can also be omitted, giving tensors in v_z rather than u_z . The tensors available from the experiment performed to extract $D_{zz}^{NL}(Z, \tau)$ are shown in Fig. 9, and summarised in Table 2.

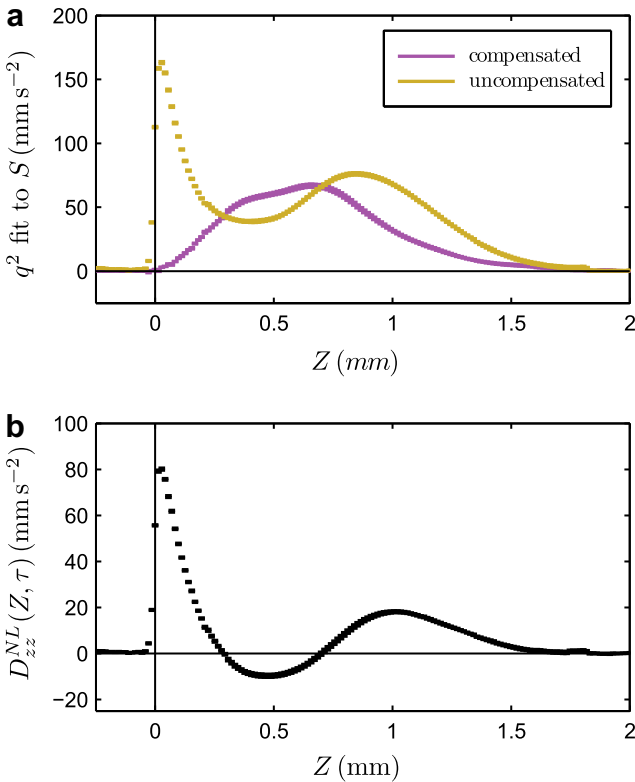


Fig. 7. The resulting fits from S_{un} and S_{comp}^c , panel (a), superposed to give $D_{zz}^{NL}(Z, \tau)$, panel (b). In this instance the difference between the uncompensated and compensated fit is large, giving small error bars.

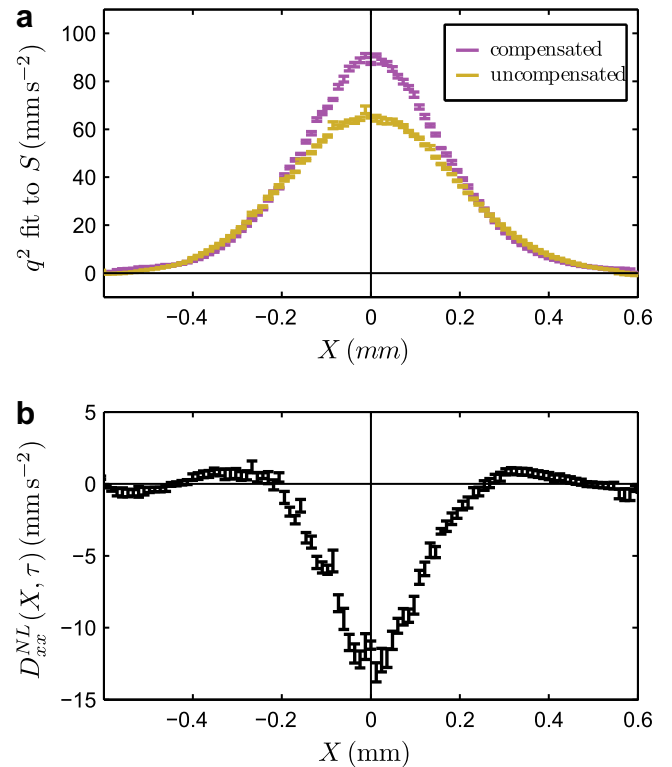


Fig. 8. The encoding for the fully transverse term $D_{xx}^{NL}(X, \tau)$ at 46.3 ms shows the small difference between the fits to the q^2 data.

4.3. Echo attenuation simulation

In order to test our experimental methodology and the associated data analysis protocols, we have carried out direct numerical calculations of the relevant dispersion tensors using a lattice-Boltzmann/Monte Carlo simulation, and then used the simulated tracer displacements to generate echo signals appropriate to the compensated and uncompensated double PGSE NMR experiments. We then process these simulated NMR data using the methods outlined above and compare the results with the directly computed tensor elements.

The simulation consists of three components, the bead pack generator, the lattice-Boltzmann (LB) flow generator, and the virtual tracer particle simulation component. These components are

Table 2

A table showing all of the displacement resolved quantities available from a pair of experiments with the initial motion encoding in the direction α , final motion encoding in the direction β and displacement encoding in the direction γ . Not all of these quantities will be non-zero. The measured quantities for a fully longitudinal encoding are shown in Fig. 9 panels (c–i).

| Description | Quantity |
|-----------------------------|---|
| Propagator | $\langle \bar{P}(X_\gamma, \tau) \rangle$ |
| Non-local dispersion tensor | $D_{\alpha\beta}^{NL}(X_\gamma, \tau)$ |
| Non-local dispersion in v | $\langle v_\alpha(0) \bar{P}(X_\gamma, \tau) v_\beta(\tau) \rangle$ |
| First moment of velocity | $\langle u_\alpha \bar{P}(X_\gamma, \tau) \rangle, \langle \bar{P}(X_\gamma, \tau) u_\beta \rangle$ |
| First moment in v | $\langle v_\alpha \bar{P}(X_\gamma, \tau) \rangle, \langle \bar{P}(X_\gamma, \tau) v_\beta \rangle$ |
| Second moment of velocity | $1/2 \langle (u_\alpha^2 \bar{P}(X_\gamma, \tau) + \langle \bar{P}(X_\gamma, \tau) u_\alpha^2 \rangle)$ |
| Second moment in v | $1/2 \langle (v_\alpha^2 \bar{P}(X_\gamma, \tau) + \langle \bar{P}(X_\gamma, \tau) v_\alpha^2 \rangle)$ |

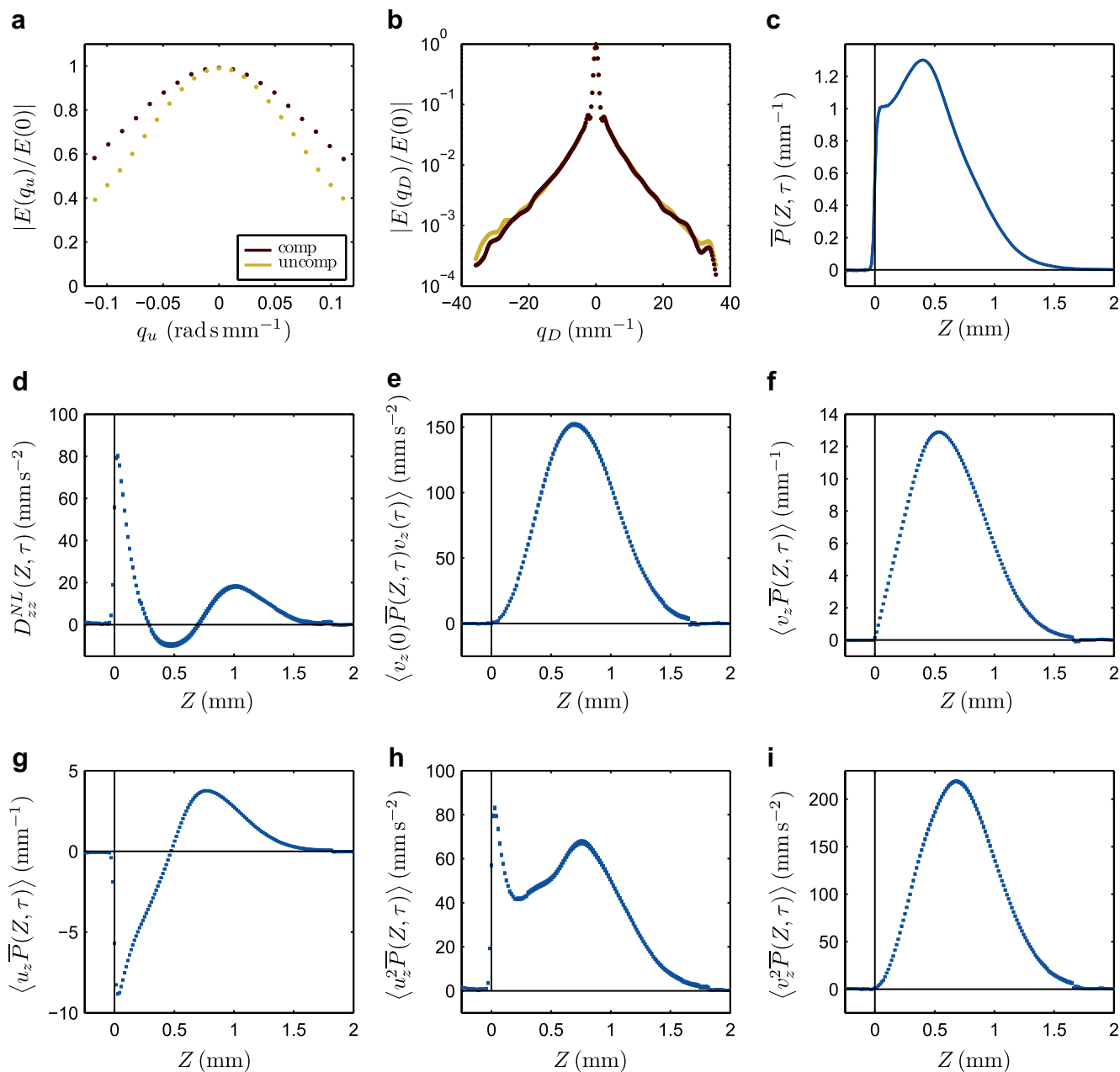


Fig. 9. A summary of the additional data from the two experiments necessary for $D_{zz}^{NL}(Z, \tau)$. Panel (a) shows the magnitude of the attenuation from the compensated and uncompensated double PGSE, the difference in the two is indicative of a positive velocity auto correlation function. Panel (b) shows the magnitude of the echo attenuation for displacement encoding for each experiment. Panel (c) shows the two identical propagators. Panel (d) gives $D_{zz}^{NL}(Z, \tau)$, for $\tau = 46.3$ ms. Panel (e) shows the non-local dispersion tensor in v rather than u . The further tensors which are able to be extracted are shown in panels (f) and (g) for the first moment resolved by displacement, and panels (h) and (i) give the second moment resolved in displacement.

combined in order to build a suitable beadpack, model the flow through it, and then model the motions of virtual tracer particles through that flow field. The code provides a way of statistically measuring the tensors we are interested in. The results between the simulated non-local dispersion in a algorithm-generated beadpack compare well with experimental measurements of a random bead pack [25] although large differences in porosities between our simulated beadpacks (~ 0.7) and experimental beadpacks (~ 0.4) preclude exact agreement. The simulated propagator of Fig. 6(c) clearly shows more slower moving particles than the experimental propagator of Fig. 9(c). These effects, and details of the simulation are discussed further in [25].

Statistical calculation of the non-local dispersion tensor is performed by calculating the contribution to the velocity auto correla-

tion function from each tracer particle and putting this value in a bin, depending on how far the tracer particle has moved. The measurement of initial and final velocity of each tracer particle can be done two ways. First, using the particles instantaneous velocity as given by its position in the local velocity field and second, by using an average velocity over some finite encoding time. The latter is similar to the experimental method where the velocity encoding is performed using a duration of Δ_u . In Fig. 10, panels (d–i) the tensors calculated using the instantaneous velocity are labelled as ‘Statistical (v)’ and the tensors calculated using a finite encoding time are labelled as ‘Statistical (Δ_u)’.

Generating the expected echo attenuation function is easily performed using the tracers in the simulation. Each particle begins the simulation with zero phase, a \mathbf{q} and \mathbf{r} dependant phase shift being

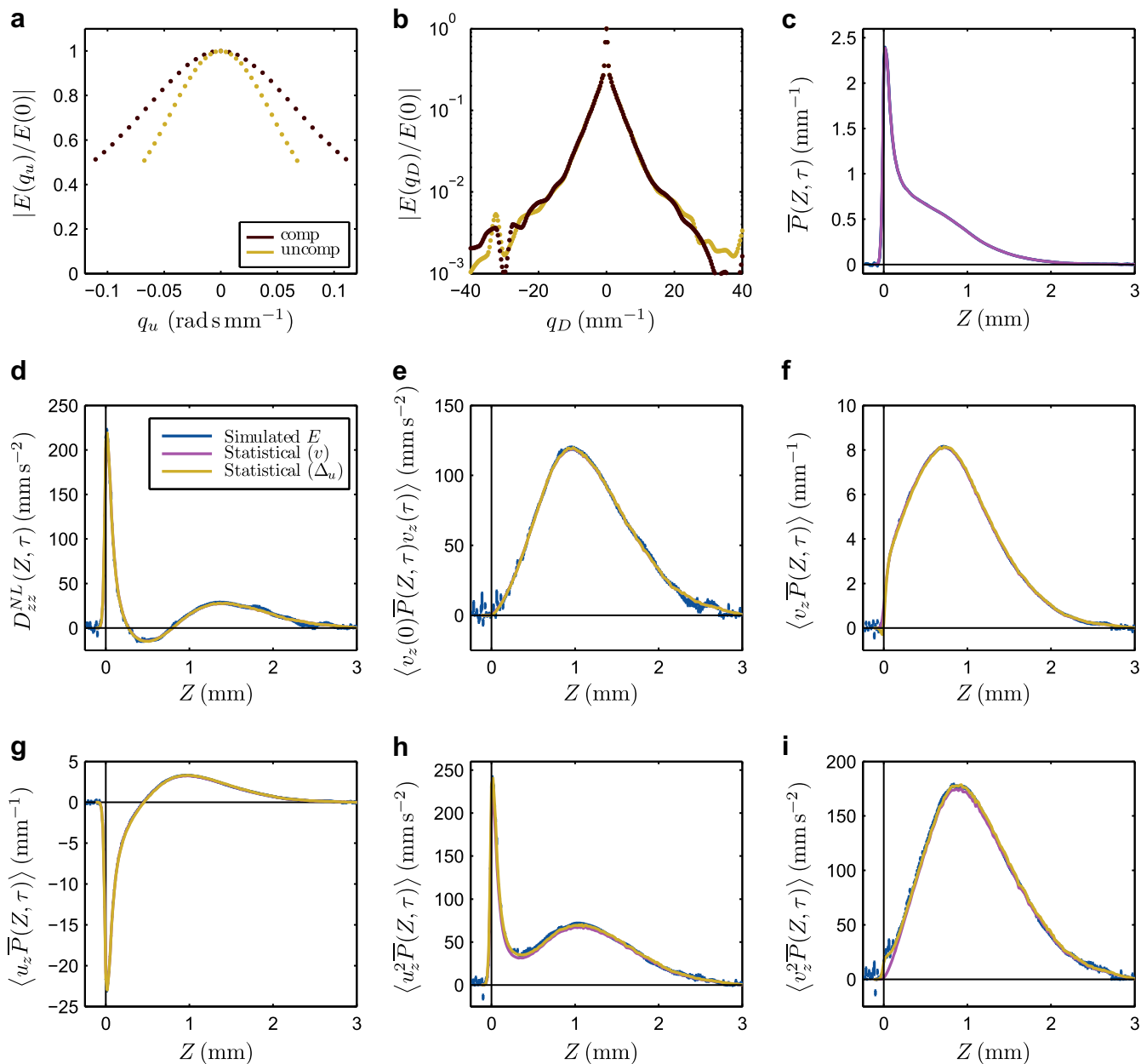


Fig. 10. A set of simulated tracer particles were used to statistically calculate all the tensors that can be measured from an experiment where the motion and displacement encoding is parallel to the flow, panels (c–i). The velocity can be measured either from the instantaneous local velocity field, ‘Statistical (v)’, or as in experiment, over a finite encoding time ‘Statistical (Δ_u)’. The same set of tracer particles were used to generate an echo attenuation function which was then processed in the manner described in the text. Panels (a) and (b) show the attenuation from the double-PGSE encoding and the displacement encoding. These tensors resulting from this analysis are labelled ‘Simulated E ’ in panels (c–i). The agreement is excellent.

added for all gradient pulses (see Fig. 1). As in the actual experiments, these phase shifts are summed over the ensemble to give an attenuation, the process being repeated for all desired values of q_u and q_D .

The procedure outlined enables verification of the interpolation in q_D , the q^2 fitting in the q_u dimension, the phase correction process and the validity of the superposition. The duration of each gradient pulse δ is not included in the simulation. Values for q_u and q are chosen to be similar to experiments. The effect of the finite encoding time, Δ_u , for velocity is also included in the echo attenuation simulation, as shown above this can also be investigated with statistical calculations. In general the simulation noise due to the low number of tracer particles is larger than experimental noise. Nevertheless, a small amount of gaussian noise is added to the simulated echo-attenuation before processing. The tensors calculated in this way are labelled in Fig. 10 as 'Simulated E '. Overall the agreement between the simulated echo attenuation and the statistical calculation is excellent. Small discrepancies can be seen due to the approximation of the instantaneous velocity over the period Δ_u , this effect is highlighted by the particles in the term $\langle v_z^2 P(Z, \tau) \rangle$ (see Fig. 6(i)) by the particles with no net displacement.

5. Conclusion

Measurement of the non-local dispersion tensor requires a pair of two-dimensional pulse sequences, each involving a single-PGSE component to measure displacements and hence correlation information, as well as a double-PGSE component to measure velocities. Data analysis involves a superposition of compensated and phase corrected uncompensated double-PGSE signals. This signal comparison often involves a small difference, requiring a consistent signal and hence a means of producing a stable flow. In the double-PGSE dimension a low- q analysis is performed. An algorithm for reliably fitting data around $q = 0$ for a wide range of attenuations is essential.

Components of the non-local dispersion tensor have been shown to be able to be measured with PGSE NMR. The robustness of our experimental protocols have been tested using simulations. Statistically calculated tensor components obtained directly from tracer migration information in the simulation are compared with those calculated by applying our data analysis protocols to simulated echo attenuation data also obtained from the tracer information. Excellent agreement is found, thus further verifying our pulse sequence and processing methodology. The superposition required is also shown to be able to recover other non-local tensors, giving further information about the first and second moments of displacement. Full details of a complete set of non-local components are presented elsewhere.

Acknowledgment

The authors are grateful to the New Zealand Foundation for Research, Science and Technology for funding support.

References

- [1] E.L. Hahn, Spin echoes, *Phys. Rev.* 80 (1950) 580–601.
- [2] H. Carr, E. Purcell, Effects of diffusion on free precession in nuclear magnetic resonance experiments, *Phys. Rev.* 94 (3) (1954) 630–638.
- [3] R.J. Hayward, K.J. Packer, D.J. Tomlinson, Pulsed field-gradient spin-echo NMR studies of flow in fluids, *Mol. Phys.* 23 (6) (1972) 1083–1102.
- [4] L. Lebon, J. Leblond, J. Hulin, N. Martys, L. Schwartz, Pulsed field gradient NMR measurements of probability distribution of displacement under flow in sphere packings, *Magn. Reson. Imaging* 14 (7–8) (1996) 989–991. 3rd International Meeting on Recent Advances in MR Applications to Porous Media, LOUVAIN, BELGIUM, SEP 03–06, 1995.
- [5] J. Seymour, P. Callaghan, Generalized approach to NMR analysis of flow and dispersion in porous media, *AICHE J.* 43 (1997) 2096–2111.
- [6] J. Bear, *Dynamics of Fluids in Porous Media*. New York: American Elsevier Publishing Company, Inc., 1972.
- [7] J. Tessier, K. Packer, The characterization of multiphase fluid transport in a porous solid by pulsed gradient stimulated echo nuclear magnetic resonance, *Phys. Fluids* 10 (1998) 75–85.
- [8] A. Sederman, M. Johns, P. Alexander, L. Gladden, Structure-flow correlations in packed beds, *Chem. Eng. Sci.* 53 (1998) 2117–2128.
- [9] B. Manz, P. Alexander, L. Gladden, Correlations between dispersion and structure in porous media probed by nuclear magnetic resonance, *Phys. Fluids* 11 (1999) 259–267.
- [10] A. Khrapitchev, P. Callaghan, Reversible and irreversible dispersion in a porous medium, *Phys. Fluids* 15 (2003) 2649–2660.
- [11] P. Callaghan, S. Codd, Flow coherence in a bead pack observed using frequency domain modulated gradient nuclear magnetic resonance, *Phys. Fluids* 13 (2001) 421–427.
- [12] M.W. Hunter, P.T. Callaghan, NMR measurement of nonlocal dispersion in complex flows, *Phys. Rev. Lett.* 99 (21) (2007) 210602–1–210602–4.
- [13] D. Koch, J. Brady, A nonlocal description of advection diffusion with application to dispersion in porous-media, *J. Fluid Mech.* 180 (1987) 387–403.
- [14] P. Callaghan, Some perspectives on dispersion and the use of ensemble-averaged PGSE NMR, *Magn. Reson. Imaging* 23 (2005) 133–137. 7th International Conference on Magnetic Resonance in Porous Media (MRPM7), Palaiseau, France, Jul 04–08, 2004.
- [15] S. Stapf, NMR investigations of correlations between longitudinal and transverse displacements in flow through random structured media, *Chem. Phys.* 284 (2002) 369–388.
- [16] S. Stapf, S. Han, C. Heine, B. Blumich, Spatiotemporal correlations in transport processes determined by multiple pulsed field gradient experiments, *Concepts Magn. Reson.* 14 (3) (2002) 172–211.
- [17] U. Tallarek, T. Scheenen, H. Van As, Macroscopic heterogeneities in electroosmotic and pressure-driven flow through fixed beds at low column-to-particle diameter ratio, *J. Phys. Chem. B* 105 (2001) 8591–8599.
- [18] S. Stapf, K. Packer, S. Bekri, P. Adler, Two-dimensional nuclear magnetic resonance measurements and numerical simulations of fluid transport in porous rocks, *Phys. fluids* 12 (2000) 566–580.
- [19] B. Manz, L. Gladden, P. Warren, Flow and dispersion in porous media: lattice-Boltzmann and NMR studies, *AICHE J.* 45 (1999) 1845–1854.
- [20] S. Stapf, K. Packer, R. Graham, J. Thovert, P. Adler, Spatial correlations and dispersion for fluid transport through packed glass beads studied by pulsed field-gradient NMR, *Phys. Rev. E* 58 (1998) 6206–6221.
- [21] A. Ding, D. Candela, Probing nonlocal tracer dispersion in flows through random porous media, *Phys. Rev. E* 54 (1996) 656–660.
- [22] H. Brenner, Dispersion resulting from flow through spatially periodic porous-media, *Philos. Trans. R. Soc. Lond. Ser. A-Math. Phys. Eng. Sci.* 297 (1430) (1980) 81–133.
- [23] R. Cotts, M. Hoch, T. Sun, J. Markert, Pulsed field gradient stimulated echo methods for improved NMR diffusion measurements in heterogeneous systems, *J. Magn. Reson.* 83 (1989) 252–266.
- [24] U. Scheven, J. Seland, D. Cory, NMR propagator measurements on flow through a random pack of porous glass beads and how they are affected by dispersion, relaxation, and internal field inhomogeneities, *Phys. Rev. E* 69 (2004) 021201–1–021201–9.
- [25] M.W. Hunter, A.N. Jackson, P.T. Callaghan, NMR measurement and lattice-Boltzmann simulation of the non-local dispersion tensor, *Phys. Fluids*, 2010, accepted for publication.